A composite electrode model for lithium-ion batteries with silicon/graphite negative electrodes

Weilong Ai[a,b,d], Niall Kirkaldy[c], Yang Jiang[c,d], Gregory Offer[c,d], Huizhi Wang[c], Billy Wu[b,d,*]

[a]*School of Civil Engineering, Southeast University, Nanjing, 211189, China*
[b]*Dyson School of Design Engineering, Imperial College London, London, SW7 2AZ, UK*
[c]*Department of Mechanical Engineering, Imperial College London, London, SW7 2AZ, UK*
[d]*The Faraday Institution, Quad One, Becquerel Avenue, Harwell Campus, Didcot, OX11 0RA, UK*

Abstract

Silicon is a promising negative electrode material with a high specific capacity, which is desirable for commercial lithium-ion batteries. It is often blended with graphite to form a composite anode to extend lifetime, however, the electrochemical interactions between silicon and graphite have not been fully investigated. Here, an electrochemical composite electrode model is developed and validated for lithium-ion batteries with a silicon/graphite anode. The continuum-level model can reproduce the voltage hysteresis and demonstrate the interactions between graphite and silicon. At high states-of-charge, graphite provides the majority of the reaction current density, however this rapidly switches to the silicon phase at deep depths-of-discharge due to the different open circuit voltage curves, mass fractions and exchange current densities. Furthermore, operation at high C-rates leads to heterogeneous current densities in the through-thickness direction, where peak reaction current densities for silicon can be found at the current collector-electrode side as opposed to the separator-electrode side for graphite. Increasing the mass fraction of silicon also highlights the beneficial impacts of reducing the peak reaction current densities. This work, therefore, gives insights into the effects of silicon additives, their coupled interactions and provides a platform to test different composite electrodes for better lithium-ion batteries.

Keywords: Composite electrode, Silicon/graphite, Voltage hysteresis, Lithium-ion batteries .

*Corresponding author.
  Email address:* `billy.wu@imperial.ac.uk` (Billy Wu)

Nomenclature

ϵ_e — volume fraction of electrolyte

ϵ_s — volume fraction of active material

κ_e — conductivity of electrolyte [S m^{-1}]

ϕ_k — potential of phase k [V]

σ_k — conductivity of phase k [S m^{-1}]

A — cell surface area [m^2]

a_s — specific surface area [m^{-1}]

b_k — Bruggeman's coefficient of phase k

c_k — concentration of lithium in phase k [mol m^{-3}]

D_k — lithium diffusion coefficient of phase k [m^2 s^{-1}]

F — Faraday constant [96485 C mol^{-1}]

I — electronic current [A]

i_0 — exchange current density [A m^{-2}]

j^{Li} — reaction current density per volume [A m^{-3}]

L — cell thickness [m]

L_k — thickness of domain k [m]

m_k — reaction rate in phase k [A m$^{2.5}$ mol$^{-1.5}$]

Q — cell capacity [Ah]

R — gas constant [8.314 J mol^{-1} K^{-1}]

R_k — particle radius of phase k [μm]

T — absolute temperature [K]

t_+^0 — transference number of lithium-ion

V_k — volume fraction in active material

Subscripts and superscripts

0 — initial parameter

avg — average parameter

de — delithiation

e — electrolyte phase

eff — effective parameter

g — parameter of graphite

li — lithiation

max — maximum value

n — negative electrode

ocp — open circuit potential

p — positive electrode

s — solid phase

sep — separator

si — parameter of silicon

surf — particle surface

typ — typical parameter

1. Introduction

Lithium-ion (Li-ion) batteries with high energy densities are desired to address the range anxiety of electric vehicles. A promising way to improve energy density is through adding silicon to the graphite negative electrode, as silicon has a large theoretical specific capacity of up to 4200 mAh g^{-1} [1]. However, there are a number of problems when introducing silicon into composite electrodes: namely increased volume change, voltage hysteresis and the complex interactions between the two phases. Compared with a ca. 10% volume change of graphite after (de)lithiation, the value can go up to ca. 400 % (theoretically) for silicon under full lithiation [1]. This large volume change can lead to large stresses in the electrode materials, resulting in particle fragmentation and loss of active materials [2]. In addition, the open circuit potential (OCP) curves of silicon are different between lithiation and delithiation, which can result in significantly different charge and discharge behaviours at the cell-level [3]. Furthermore, because silicon particles rapidly fracture during cycling, the amount of silicon is normally limited to a small mass fraction, relative to graphite, in the negative electrode for commercial battery cells, e.g. ca. 10 % for the LG M50 cells [4]. Thus, physics-based models, which capture the non-linear interactions between the two phases, are needed in-order to better understand the dynamic behaviour of these composite electrodes. This includes understanding how the reaction current density is split between the two phases during operation which impacts electrode utilisation and lifetime.

Previous studies have sought to understand the degradation mechanisms of silicon electrode particles and to build up theoretical models. Experiments have shown that the fracture of silicon nanoparticles is size-dependent, where Liu et al. [5] reported a critical diameter of ca. 150 nm for no cracks upon first lithiation. The fracture energy of pure silicon was measured to be around 8 J m^{-2} and essentially independent of the degree of lithiation [6]. Theoretical models at particle level have been developed to account for the plasticity [7] and elasto-plasticity [8] of silicon, where it was demonstrated that fracture can be averted for small particle sizes and yield strengths, by increasing the elastic modulus. Atomistic simulations for fracture of pure silicon reveal a transition from intrinsic nanoscale cavitation to extension shear banding ahead

of the crack tip [9].

The voltage hysteresis in silicon is caused by the different phases which form during lithiation and delithiation. For instance, a new crystalline phase ($Li_{15}Si_4$) was reported to form when silicon is lithiated to below 50 mV [10], where all potentials quoted in this work are versus Li/Li^+. Subsequently, delithiation of the $Li_{15}Si_4$ phase leads to a potential plateau at 0.4 V, which is different from the lithiation process of silicon, and its shape is affected by lithiation depth [10] and silicon particle size [11]. A thermodynamic model has been developed by Verbrugge et al. [12, 13] for the electrochemical reactions and resulting OCP of silicon. Multi-step phase transformation of silicon has also been modelled to handle the amorphization process under deeper lithiation to nearly 0 V [14]. In addition to the phase changes of silicon electrodes, different stress states between lithiation and delithiation can also lead to voltage hysteresis [15, 16]. This OCP hysteresis thus varies the electrochemical behaviour of silicon between charge and discharge.

A composite anode consisting of silicon and graphite can make use of the advantages of both materials, and has been tested for half and full cells [17]. Different types of composite structures have been developed, with layers of silicon encasing a graphite core or embedding silicon powders into graphite particles [18]. The swelling and contraction of silicon produces voids and gaps with surrounding materials, leading to loss of electrical contact and degradation [18, 19]. Other structures/morphologies include carbon coated silicon particles [20, 21] or nanoscale architectural structures of silicon/graphite composites [22]. Experiments show that increasing the amount of silicon can improve the cell capacity but with a cost of greater capacity loss [23, 24]. Highly adhesive binders (containing high content of catechol groups) can alleviate the pulverization of silicon/graphite composite electrode [25]. Pre-lithiation can compensate the active lithium loss of silicon/graphite composite electrode in the first cycle, while the homogeneity of lithiation is affected by the silicon particle size [26]. However, the modeling of silicon/graphite composite electrodes remains challenging, because of the complex lithiation mechanisms of silicon. One attempt is the one dimensional composite half-cell model [27], where the porosity change of the electrode was considered as a result of the silicon deformation. The interplay between silicon and graphite was modelled using a core-shell structure [28] to

4

study the influence of silicon on the stress and volume change. Work by Jung et al. [29] demonstrated a blended electrode model which was considered the positive electrode though did not include the silicon thermodynamics. Order reduced model for composite electrodes were developed using the single particle model, while the current splits between two active materials remain challenging and are approximated through iterations [30–32]. The electronic connections between composite electrodes and the conductive matrix are modelled using an equivalent-circuit model to describe the film resistance and the contact resistance [33]. Nevertheless, the electrochemical interactions between silicon and graphite have not been fully understood. Therefore, there is a need for a composite electrode model to capture the electrochemical interactions of silicon and graphite.

In this work, an electrochemical blended electrode model is developed for silicon and graphite composites at the continuum cell-level. A brief review on chemical reactions of silicon and its oxides is given in Section 2. The governing equations of the composite electrode model are presented in Section 3. Then, the model is used to investigate the electrochemical interactions between silicon and graphite, nonuniform interfacial current densities across the negative electrode and the effect of different mass fractions of silicon in Section 4, followed by a summary in Section 5.

2. (De)lithiation of silicon and its oxides

Because of the poor cycle stability of pure silicon, silicon oxides are often used in commercial Li-ion battery cells, to reduce the rate of capacity degradation.

Silicon has reaction pathways as shown in Fig. 1. There are two phase changes (marked as (1) and (2)) in the reactions of silicon when the voltage is above 0.05 V vs Li/Li$^+$. The first step is from a-Si to a-Li$_x$Si, where "a" represents an amorphous phase. By contrast, the second step forms the final amorphous product of a-Li$_{15}$Si$_4$. Incremental capacity analysis of Si negative electrodes reveals two separate peaks during lithitation, corresponding to these two steps. [13]. When the voltage of Si is below 0.05 V vs Li/Li$^+$, a crystalline phase is generated from a-Li$_{15}$Si$_4$ [14]. This process involves a preceding nucleation step (f3) for a-Li$_{15+\delta}$Si$_4$, a subsequent grain growth step (f4) for c-Li$_{15}$Si$_4$ during lithiation and an amorphization step (b2)
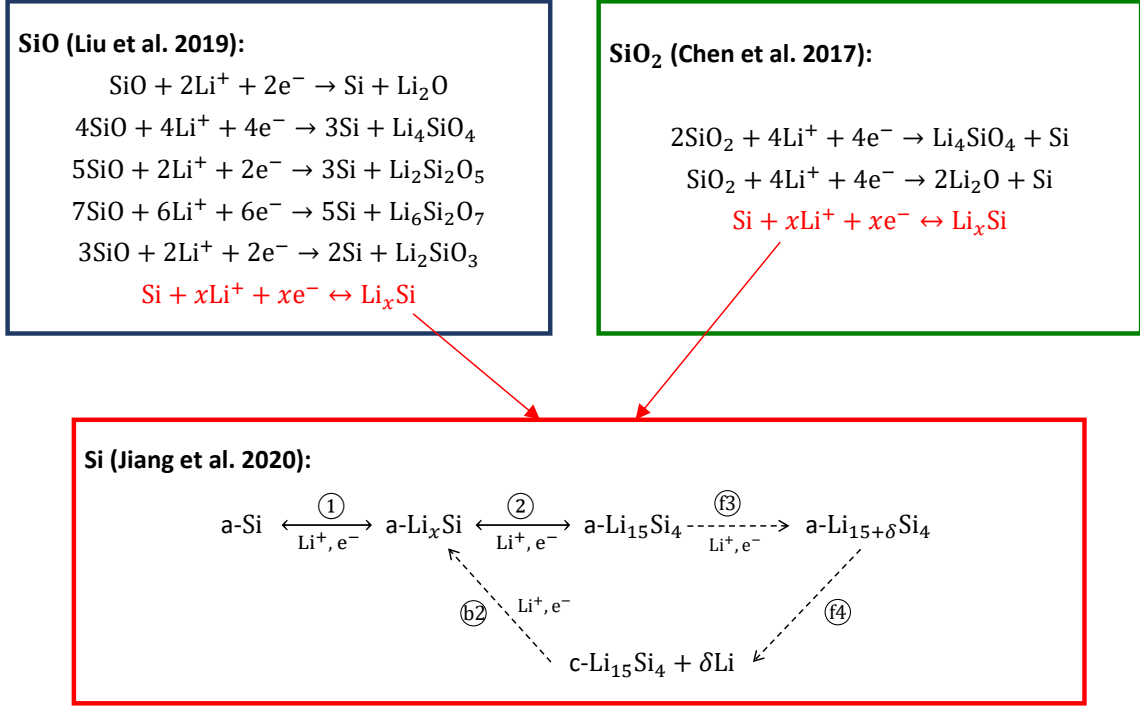
5

Figure 1: The reactions of silicon [14], silicon oxide [1] and silicon dioxide [34].

for c-$Li_{15}Si_4$ returning to a-Li_xSi during delithiation. δ represents a very small amount of Li, which acts as catalyst for activating the crystallization of a-$Li_{15+\delta}Si_4$. Comparing the two reversible reactions (① and ②) for a-$Li_{15}Si_4$, the reactions ③, ④ and ⑤ for c-$Li_{15}Si_4$ are unidirectional, leading to a significant difference in the voltage curves between lithiation and delithiation.

Silicon dioxide is one of the most abundant materials on earth, found in quartz, diatoms and rice husk. Although SiO_2 has a high theoretical capacity of up to 1965 mAh/g [34], bulk SiO_2 shows less electrochemical activity towards Li due to its low Li^+ diffusivity and poor electrical conductivity. SiO_2 has two irreversible reactions in Fig. 1 forming Si, Li_4SiO_4 and Li_2O.

Silicon oxide is regraded as a random mixture of Si and SiO_2. The theoretical reversible capacity of SiO is 2680 mAh/g with a volume change of ca. 200 %, however, in experiments it delivers a capacity of 1260 mAh/g with a capacity retention of 86.5 % after 50 cycles [1]. During the first lithiation of SiO, several products are formed, including Li_xSi alloys, lithium

silicates (Li_4SiO_4, $Li_2Si_2O_5$, $Li_6Si_2O_7$, Li_2SiO_3) and Li_2O, as shown in Fig. 1. Only the extraction/insertion of Li^+ in Li_xSi alloys is reversible, while other products are generally irreversible phases.

A mixture of Si, SiO and SiO_2 is generally used for negative electrode materials. The capacity is promoted with the increase of Si, but this also leads to a lower coulombic efficiency and more capacity degradation [23, 24]. SiO_x electrodes undergo irreversible reduction reactions during the first cycle, and all subsequent cycles are in fact dominated by Si (de)lithiation (Fig. 1). Therefore, it is essential to consider the Si reactions in the negative electrode with Si or SiO_x additives.

3. Method: composite electrode model

We demonstrate a composite electrode model for silicon and graphite in this work, which could easily be adapted to study positive composite electrodes. The model is based on the Pseudo-2D Newman battery model [35], which has been widely used for Li-ion batteries and is summarised in Table 1. These equations describe the ionic transport and diffusion in the through plane direction of the separator, anode and cathode, assuming other directions are homogeneous. The (de)lithiation follows the Butler-Volmer equation with solid-phase diffusion defined by Fick's law.

Compared to the traditional Newman battery model which assumes a single spherical particle at each node in the electrode phases, the composite electrode model differs by having two spherical particles at the nodes of the negative electrode to make a composite, as shown in Fig. 2. This structure is developed from experimental observations using energy-dispersive X-ray spectroscopy (EDS) [4], where silicon is found to be surrounded by graphite, in a two phase mixture arrangement (Fig. 2). The lithium diffusion equations in silicon and graphite are thus modified to:

$$\frac{\partial c_{si}}{\partial t} = \frac{D_{si}^{eff}}{r_{si}^2} \frac{\partial}{\partial r_{si}} \left(r_{si}^2 \frac{\partial c_{si}}{\partial r_{si}} \right) \tag{1a}$$

$$\frac{\partial c_{g}}{\partial t} = \frac{D_{g}^{eff}}{r_{g}^2} \frac{\partial}{\partial r_{g}} \left(r_{g}^2 \frac{\partial c_{g}}{\partial r_{g}} \right) \tag{1b}$$

Table 1: Pseudo-2D battery model equations [35].

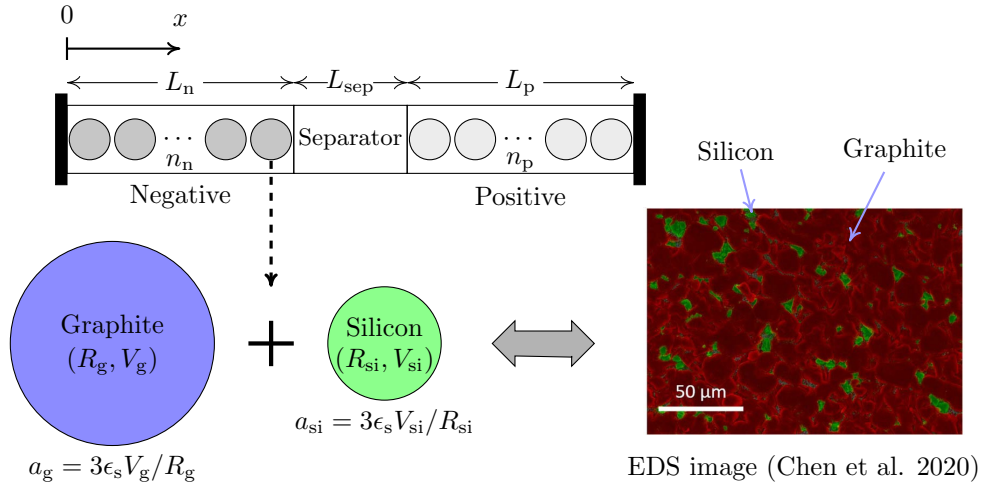| Conservation equations		Boundary Conditions
Species, electrolyte phase	$\frac{\partial \epsilon_e c_e}{\partial t} = \frac{\partial}{\partial x}\left(D_e^{\text{eff}} \frac{\partial}{\partial x} c_e\right) + \frac{1-t_+^0}{F} j^{\text{Li}}$	$\frac{\partial c_e}{\partial x}\big|_{x=0} = \frac{\partial c_e}{\partial x}\big|_{x=L} = 0$
Species, solid phase	$\frac{\partial c_s}{\partial t} = \frac{D_s}{r^2} \frac{\partial}{\partial r}\left(r^2 \frac{\partial c_s}{\partial r}\right)$	$\frac{\partial c_s}{\partial r}\big|_{r=0} = 0, -D_s \frac{\partial c_s}{\partial r}\big|_{r=R_s} = \frac{j^{\text{Li}}}{a_s F}$
Charge, electrolyte phase	$\frac{\partial}{\partial x}\left(\kappa^{\text{eff}} \frac{\partial}{\partial x} \phi_e\right) + \frac{\partial}{\partial x}\left(\kappa_D^{\text{eff}} \frac{\partial}{\partial x} \ln c_e\right) + j^{\text{Li}} = 0$	$\frac{\partial \phi_e}{\partial x}\big|_{x=0} = \frac{\partial \phi_e}{\partial x}\big|_{x=L} = 0$
Charge, solid phase	$\frac{\partial}{\partial x}\left(\sigma^{\text{eff}} \frac{\partial}{\partial x} \phi_s\right) = j^{\text{Li}}$	$-\sigma_-^{\text{eff}} \frac{\partial \phi_s}{\partial x}\big|_{x=0} = \sigma_+^{\text{eff}} \frac{\partial \phi_s}{\partial x}\big|_{x=L} = \frac{I}{A}$
		$\frac{\partial \phi_s}{\partial x}\big|_{x=L_n} = \frac{\partial \phi_s}{\partial x}\big|_{x=L_n+L_{\text{sep}}} = 0$
Bulter-Volmer kinetics	$j^{\text{Li}} = 2 a_s i_0 \sinh\left[\frac{0.5F}{RT}(\phi_s - \phi_e - \phi_{\text{ocp}})\right]$	

Figure 2: Modified Pseudo-2D battery model for the composite negative electrode of graphite and silicon. The EDS image is for the surface of the negative electrode from Chen et al. [4].

where D^{eff} is the effective diffusion coefficient, c is lithium concentration, r is the radius and t is time. The subscripts "si" and "g" represent variables for silicon and graphite, respectively. These two equations have boundary conditions as follows

$$\frac{\partial c_{\text{si}}}{\partial r_{\text{si}}}\Big|_{r_{\text{si}}=0} = 0 \quad D_{\text{si}}^{\text{eff}} \frac{\partial c_{\text{si}}}{\partial r_{\text{si}}}\Big|_{r_{\text{si}}=R_{\text{si}}} = -\frac{j_{\text{si}}^{\text{Li}}}{a_{\text{si}} F} \tag{2a}$$

$$\frac{\partial c_g}{\partial r_g}\Big|_{r_g=0} = 0 \quad D_g^{\text{eff}} \frac{\partial c_g}{\partial r_g}\Big|_{r_g=R_g} = -\frac{j_g^{\text{Li}}}{a_g F} \tag{2b}$$

where F is the Faraday constant, R_{si} and R_{g} are the radii of the silicon and graphite electrode particles, respectively. The surface to volume ratios of silicon a_{si} and graphite a_{g} are given by

$$a_{\text{si}} = 3V_{\text{si}}\epsilon_{\text{s}}/R_{\text{si}} \tag{3a}$$

$$a_{\text{g}} = 3V_{\text{g}}\epsilon_{\text{s}}/R_{\text{g}} \tag{3b}$$

where ϵ_{s} is the volume fraction of active materials, V_{si} and V_{g} are the relative volume fractions of silicon and graphite in the active materials respectively, with $V_{\text{si}} + V_{\text{g}} = 1$. The reaction current densities per volume of silicon $j_{\text{si}}^{\text{Li}}$ and graphite j_{g}^{Li} are respectively

$$j_{\text{si}}^{\text{Li}} = 2a_{\text{si}}i_{\text{si},0}\sinh\left[\frac{0.5F}{RT}(\phi_{\text{s}} - \phi_{\text{e}} - \phi_{\text{si,ocp}})\right] \tag{4a}$$

$$j_{\text{g}}^{\text{Li}} = 2a_{\text{g}}i_{\text{g},0}\sinh\left[\frac{0.5F}{RT}(\phi_{\text{s}} - \phi_{\text{e}} - \phi_{\text{g,ocp}})\right] \tag{4b}$$

with R the gas constant, T temperature, ϕ_{s} potential in the solid phases and ϕ_{e} potential in the electrolyte. The exchange current densities for silicon $i_{\text{si},0}$ and graphite $i_{\text{g},0}$ are respectively defined as

$$i_{\text{si},0} = m_{\text{n}}\sqrt{c_{\text{e}}c_{\text{si,surf}}(c_{\text{si,max}} - c_{\text{si,surf}})} \cdot \frac{c_{\text{g,max}}}{c_{\text{si,max}}} \tag{5a}$$

$$i_{\text{g},0} = m_{\text{n}}\sqrt{c_{\text{e}}c_{\text{g,surf}}(c_{\text{g,max}} - c_{\text{g,surf}})} \tag{5b}$$

where $c_{\text{si,max}}$ and $c_{\text{g,max}}$ are the maximum lithium concentration in silicon and graphite respectively. m_{n} is the reaction rate of the negative electrode, measured by Chen et al. [4] for the LG M50 cell. Considering silicon has a larger maximum lithium concentration than graphite, the exchange current density of silicon is rescaled by $c_{\text{g,max}}/c_{\text{si,max}}$ in order to normalise the expression under the square root in Eq. (5).

$\phi_{\text{si,ocp}}$ and $\phi_{\text{g,ocp}}$ are the equilibrium potential functions of silicon and graphite, respectively, which are fitted functions from Fig. A1 (a) in this work. The voltage hysteresis in silicon is obtained by the sigmoid function, i.e. $\text{sigmoid}(x) = [1 + \sinh(x)]/2$, which switches between the

OCP functions of delithiation $\phi_{\text{si,ocp}}^{\text{de}}$ and lithiation $\phi_{\text{si,ocp}}^{\text{li}}$, according to the current direction,

$$\phi_{\text{si,ocp}} = \text{sigmoid}\left(-\frac{100I}{Q}\right)\phi_{\text{si,ocp}}^{\text{de}} + \text{sigmoid}\left(\frac{100I}{Q}\right)\phi_{\text{si,ocp}}^{\text{li}} \tag{6}$$

where I is the applied current and Q is the cell capacity. The coefficient 100 is introduced to rescale the applied current (normalised by the cell capacity) and affects the switching speed between the two OCP functions of silicon. Several coefficients were tested, with the value 100 providing a rapid switch whilst not causing convergence issues.

At the electrode level, the interfacial current density per volume of the composite j^{Li} is made up of contributions from silicon and graphite, following

$$j^{\text{Li}} = j_{\text{si}}^{\text{Li}} + j_{\text{g}}^{\text{Li}} \tag{7}$$

In the charge transport equation, silicon and graphite are assumed to have the same potential, considering they have good electrical conductivity. By contrast, their equilibrium potentials are determined by the lithium concentration on the surface of electrode particles and are therefore normally different. The interactions between silicon and graphite are obtained through their reactions with the electrolyte in Eq. (7), rather than direct reactions between the two active materials [29], which introduce additional parameters, e.g. the interaction reaction rates and contact surface areas, and are difficult to measure. Another alternative is to define multiple reaction currents for the different active materials, but this suffers from numerical instabilities, when the magnitude or direction of the current is changed abruptly [31], and adds additional parameterisation complexity.

4. Results and analysis

The capabilities of the composite electrode model are demonstrated using the commercial battery cell LG M50T, a new version of the cell LG M50, with a silicon/graphite composite negative electrode and a nickel-manganese-cobalt (NMC) 811 positive electrode. Its parameters are similar to ones of the LG M50 from Chen et al. [4] and are listed in Table 2. Additional

Table 2: Parameters of the LG M50 cell [4].

Parameter	Description	Negative electrode	Separator	Positive electrode
L_k	Thickness [μm]	85.2	12	75.6
ϵ_e	Electrolyte volume fraction [%]	25	47	33.5
ϵ_k	Active material volume fraction [%]	75	-	66.5
b_k	Bruggeman coefficient	2.91	2.57	2.43
$c_{\max}$	Maximum lithium concentration [mol m^{-3}]	-	-	63,104
c_0	Initial lithium concentration [mol m^{-3}]	-	-	17,038
σ_k	Electrode conductivity [S m^{-1}]	215	-	0.18
D_k	Electrode Diffusivity [m^2 s^{-1}]	-	-	4×10^{-15}
R_k	Particle radius [μm]	-	-	5.22
m_k	Reaction rate [A m$^{2.5}$ mol$^{-1.5}$]	6.48×10^{-7}	-	3.42×10^{-6}
c_e^{typ}	Typical lithium concentration in electrolyte [mol m^{-3}]		1×10^3	
D_e^{typ}	Typical electrolyte diffusivity [m^2 s^{-1}]		5.34×10^{-10}	
κ_e^{typ}	Typical electrolyte conductivity [S m^{-1}]		1.1	
t_+^0	Transference number		0.2594	

parameters for the silicon and graphite electrode particles are presented in Table 3. Here, the relative volume fraction of silicon is set to 2 % (and 98 % for graphite), following an iterative approach, to match the capacity of the composite negative electrode. This is lower than the 10 % reported in Chen et al. [4] as this measurement was made from surface energy dispersive X-ray spectroscopy images of the negative electrode and may not be a fair estimation of the mass fraction of silicon through the entire electrode. Then, the initial lithium concentrations of graphite and silicon are calculated from the initial lithium concentration of the composite negative electrode from Chen et al. [4]. The cell has a constant temperature $T = 298$ K in all simulations. The model is validated against experimental data, and then three groups of simulations are carried out to study the electrochemical interactions between silicon and graphite, the non-uniform interfacial current densities across the negative electrode and different volume fractions of silicon, in the following sections.

Table 3: Additional parameters of graphite and silicon (* estimation).

Parameter	Description	Graphite	Silicon
c_{max}	Maximum lithium concentration [mol m^{-3}]	28,700 [36]	278,000 [28]
c_0	Initial lithium concentration [mol m^{-3}]	$23,000^*$	$275,220^*$
V_k	Volume fraction in active material	0.98^*	0.02^*
R_k	Particle radius [µm]	5.86 [4]	1.52 [4]
D_k	Diffusivity [m^2 s^{-1}]	5.5×10^{-14} [36]	1.67×10^{-14} [28]

4.1. Validation

The cell is tested under a discharge rate of C/100 till the voltage reaches 2.5 V, followed by a 1 h rest and C/100 charge to 4.2 V. The corresponding experimental procedures are detailed in Appendix B. The cell voltage is given in Fig. 3 (a), which shows this model can successfully reproduce the voltage hysteresis and agrees well with the experimental results [4]. Under this small current (C/100), the battery system is under quasi-equilibrium, so silicon and graphite have approximately equal equilibrium potentials, which match well the experimental measurements for the electrode as a composite in Fig. 3 (b). Here, the averaged equilibrium potential over the negative electrode is obtained using $\frac{1}{L_n} \int_{L_n} \phi_k \mathrm{d}L_n$. From Fig. 3 (c), the averaged lithium concentration (over the negative electrode) varies non-linearly between the graphite and silicon, with the (de)lithiation current density greater for graphite at high SOCs, but with the silicon lithiation state rapidly changing at low SOCs. The difference of lithium concentration between delithiation and lithiation in silicon originates from the voltage hysteresis.

We then investigate three higher C-rates of discharge, including 0.5, 1 and 1.5 C. The cell voltages are presented in Fig. 3 (d), which show fair agreement with experimental results from Chen et al. [4]. The deviation in cell voltage at low SOCs was attributed to the constant diffusion coefficient used in this work, while its value can vary by two orders of magnitude at different SOCs in reality [4]. In addition, the phase changes in silicon are not considered in the model and are simplified using the OCP functions in Fig. A1. However, despite these simplifications, the proposed composite electrode model can replicate the voltage hysteresis and the cell voltage variations for the LG M50T cells. These results support the mixed poten-
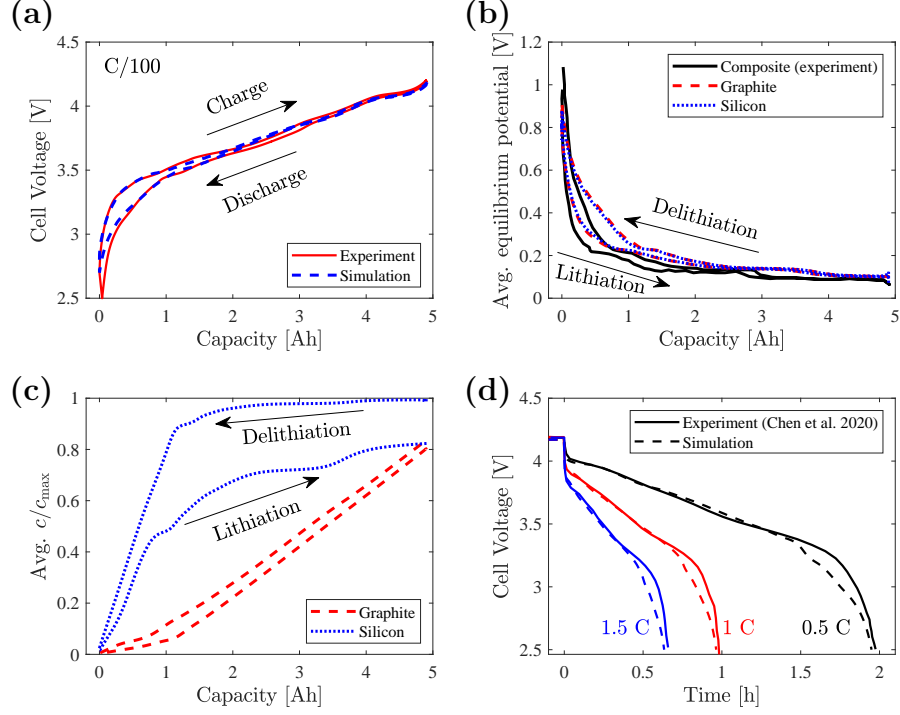
Figure 3: Validation of the proposed composite electrode model: under C/100 for (a) cell voltage, (b) averaged equilibrium potential over the negative electrode and (c) averaged lithium concentration in silicon and graphite; (d) cell voltage under 0.5 C, 1 C and 1.5 C discharge.

tial phenomenon occurring in composite electrodes, which has not been reported by previous theoretical studies ignoring the two simultaneous kinetic reactions of silicon and graphite.

4.2. Interactions between silicon and graphite

The C/100 (dis)charge cycle is used to investigate the electrochemical interactions between silicon and graphite. The averaged equilibrium potentials and interfacial current densities per area of graphite and silicon, i.e. $j_{\mathrm{g}}^{\mathrm{Li}}/a_{\mathrm{g}}$ and $j_{\mathrm{si}}^{\mathrm{Li}}/a_{\mathrm{si}}$, are presented in Fig. 4 (a-d). At high SOCs, the reaction current density and electrochemical behaviour is mostly dominated by graphite, however, at low SOCs, the silicon starts to output the majority current density. The magnitude of the silicon reaction current density is significantly higher than that of the graphite phase, due to the lower volume fraction (2 %), and thus surface area, of silicon for the same current density. From discharge to rest, the equilibrium potential of silicon has an instantaneous drop, as shown in Fig. 4 (c), because of the voltage hysteresis of silicon. The decrease of silicon equilibrium potential leads to a voltage difference between silicon and graphite and drives an

interacting current from silicon to graphite in Fig. 4 (d), to balance their potentials. There is no interacting current during the rest period, when silicon and graphite have the same equilibrium potential. Similar interacting currents can be found between silicon and graphite when the cell changes from rest to charge as given in Fig. 4.
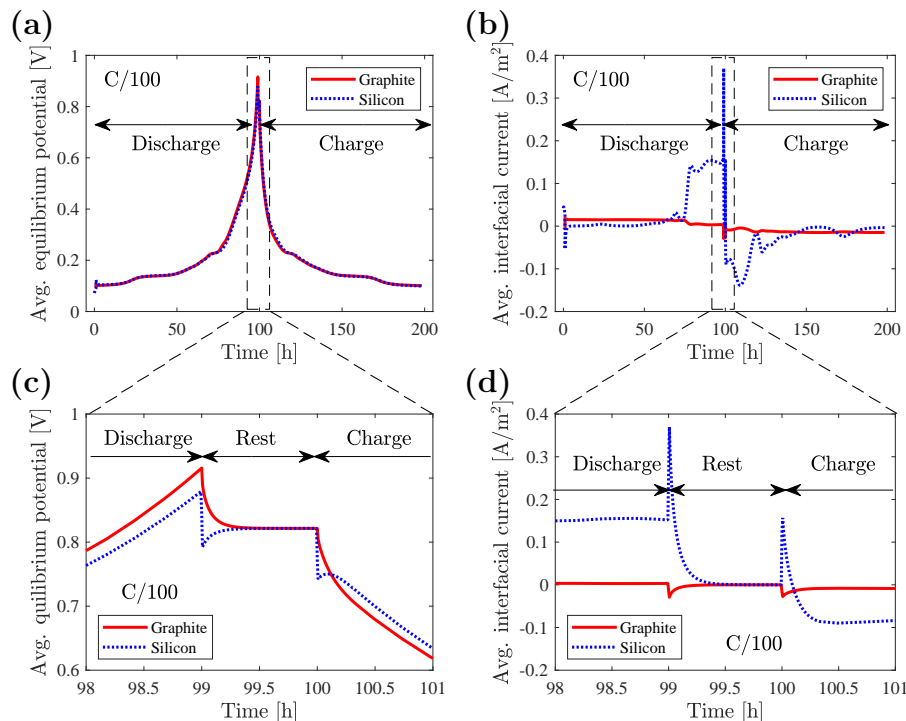

Figure 4: Electrochemical interactions between silicon and graphite at the electrode level: (a) averaged equilibrium potential and (b) averaged interfacial current density per area with (c-d) the zoom in views of the dashed region respectively.

The mechanism of the interactions between silicon and graphite can be further illustrated in Fig. A1 (b-c). From the incremental capacity analysis in Fig. A1 (b), peaks occur at the potentials of 0.1 and 0.15 V for graphite, which are lower than 0.3 and 0.5 V for silicon under delithiation. By contrast, silicon under lithiation has peaks at the same potential as graphite. In addition, silicon under delithiation has more phase change reactions at low SOCs, as indicated by less steep curves in Fig. A1 (c). Therefore, silicon is more active at low SOCs, while graphite goes through most phase changes at high SOCs. The voltage hysteresis of silicon leads to asymmetric interacting currents between silicon and graphite, when there is a change in the applied cell-level current.
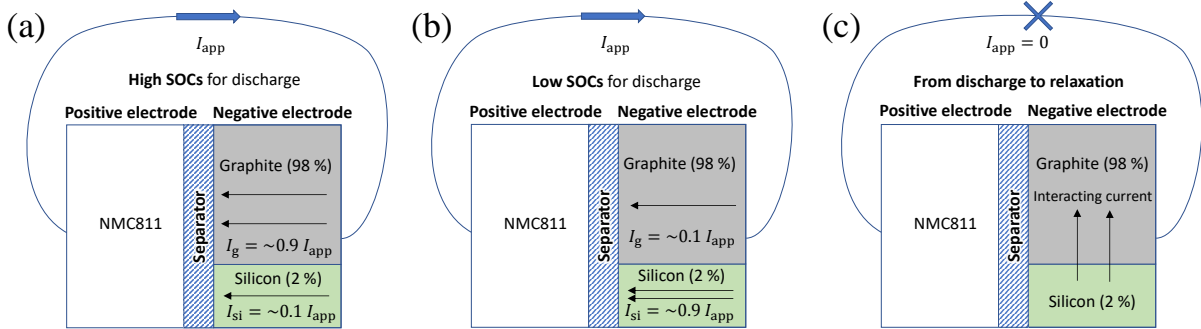
Figure 5: The schematic of the electrochemical interactions between silicon and graphite: (a) high SOCs and (b) low SOCs in discharge and (c) relaxation after discharge.

At the cell-level, the interactions between silicon and graphite are summarised in Fig. 5 (a-c). At the beginning of discharge, graphite delivers the majority of the current in the negative electrode in Fig. 5 (a), because it has a lower potential plateau then silicon. At low SOCs in Fig. 5 (b), silicon reaches its potential plateau and starts to dominate the reaction current, while graphite has passed all potential plateaus. For relaxation after discharge, there is instantaneous interaction current from silicon to graphite, as shown in Fig. 5 (c), which is due to the voltage hysteresis of silicon when the cell-level current is changed and also the different SOCs of the phases.

4.3. Local reaction current

To study the local activities of the electrode materials, we compare the cell behaviour during discharge at 2C. The distributions of interfacial current density per area, i.e. j_k^{Li}/a_k, across the negative electrode are given in Fig. 6 (a). At $t = 0.1$ h, the interfacial current density in graphite is almost two times larger at the separator side than at the current collector. Silicon is not active at high SOCs, so interfacial current densities in silicon are small at the beginning of discharge. By contrast at $t = 0.46$ h, the interfacial currents in graphite become small, and silicon starts to deliver more current. In contrast to graphite, silicon has larger interfacial current densities at the current collector than at the separator side by the end of discharge, as shown in Fig. 6 (a).

This phenomenon can be explained by the lithium concentration and equilibrium potential in silicon and graphite. A non-uniform distribution of lithium in graphite can be found in Fig. 6
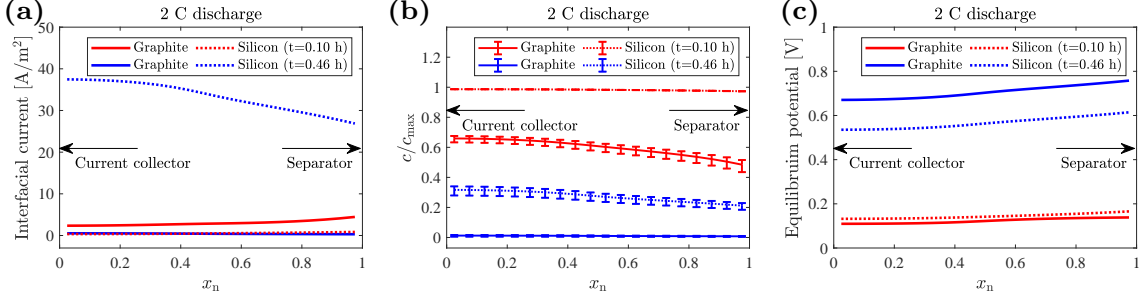
15

Figure 6: Local activities of silicon and graphite across the negative electrode: (a) interfacial current, (b) lithium concentration, (c) equilibrium potential at $t = 0.1$ h and $t = 0.46$ h for 2 C discharge. Error bars indicate the variation of lithium concentration in particles.

(b) at $t = 0.1$ h, where the bars represent the variation of lithium concentration at particle level, i.e. the upper and lower bars represent the lithium concentration at the centre and at the surface of the particle, respectively. The separator side has lower lithium concentration and bigger variation than the current collector side. Silicon has small interfacial currents, so lithium concentration is almost uniformly distributed and remains the initial concentration. Towards the end of discharge ($t = 0.46$ h), the lithium concentration in graphite becomes nearly zero. Silicon has higher lithium concentration for $c/c_{\max} = 0.3$ at the current collector versus $c/c_{\max} = 0.2$ at the separator side, leading to a higher exchange current rate in silicon close to the current collector. In addition, silicon and graphite have similar equilibrium potentials at the beginning of discharge ($t = 0.1$ h), but graphite has higher equilibrium potential than silicon at the end of discharge ($t = 0.46$ h) in Fig. 6 (c). Both lithium concentration and equilibrium potential affect the interfacial current density, according to Eq. (4). Therefore, the nonuniform distributions of lithium concentration and equilibrium potential in silicon and graphite lead to the heterogeneity of interfacial current densities across the negative electrode.

4.4. Volume fraction of silicon

The influence of silicon on cell performance is further explored with a consideration of various ratios between silicon and graphite. Different volume fractions of silicon are used, including $V_{\text{si}} = 0.001, 0.01, 0.02, 0.04, 0.06, 0.08$ and 0.1, while the volume fraction of graphite is $1 - V_{\text{si}}$ and the other components are not changed. The cell voltages of all cases are given in Fig. 7 (a), where the output voltage performance of the cell is improved by increasing the volume

fraction of silicon. Fig. 7 (b) presents the variation of averaged lithium concentration in silicon, where it decreases more slowly with increasing silicon. Averaged lithium concentration in silicon varies only at low SOCs and is independent on the fraction of silicon at high SOCs. There is little influence on the averaged interfacial current densities per area in graphite from increasing silicon in Fig. 7 (c), but the peak interfacial current density in silicon is decreased by 90 %. This is because silicon delivers the majority of the current at low SOCs, and the specific surface area of silicon increases with raising the silicon volume fraction, as given in Eq. (3).

In some batteries, a composite anode of Si, SiO and SiO_2 is used. Here a similar modelling framework, to the one proposed in this work, could be used to understand the electrode's behaviour, however the authors highlight the additional complexity of the different reaction pathways (highlighted in Fig. 1). Here SiO and SiO_2 reactions can both form Si products and thus understanding around the electrochemical performance of these multi-phase composite systems is first needed.

This work highlights the benefits of silicon additives from a physics-based battery model and sheds light to order-reduced battery models using machine learning approaches [37, 38], on ways of considering the complex reactions between multiple active materials inside lithium-ion batteries.

5. Summary

A composite electrode model has been developed for lithium-ion battery cells with a negative electrode of silicon and graphite. The electrochemical interactions between silicon and graphite are handled by two parallel functions for lithium diffusion in silicon and graphite, with separate interfacial current densities from each phase. The voltage hysteresis in silicon is modelled by combining the OCP functions of delithiation and lithiation using the sigmoid function. The proposed model successfully reproduces the voltage hysteresis at cell-level. The results demonstrate the complex interacting currents between silicon and graphite, where the two phases follow different (de)lithiation paths and have different potentials. The lithium concentration gradients and different voltage profiles of silicon and graphite lead to nonuniform distributions of the interfacial current density. At high SOCs, the graphite phase contributes the majority of
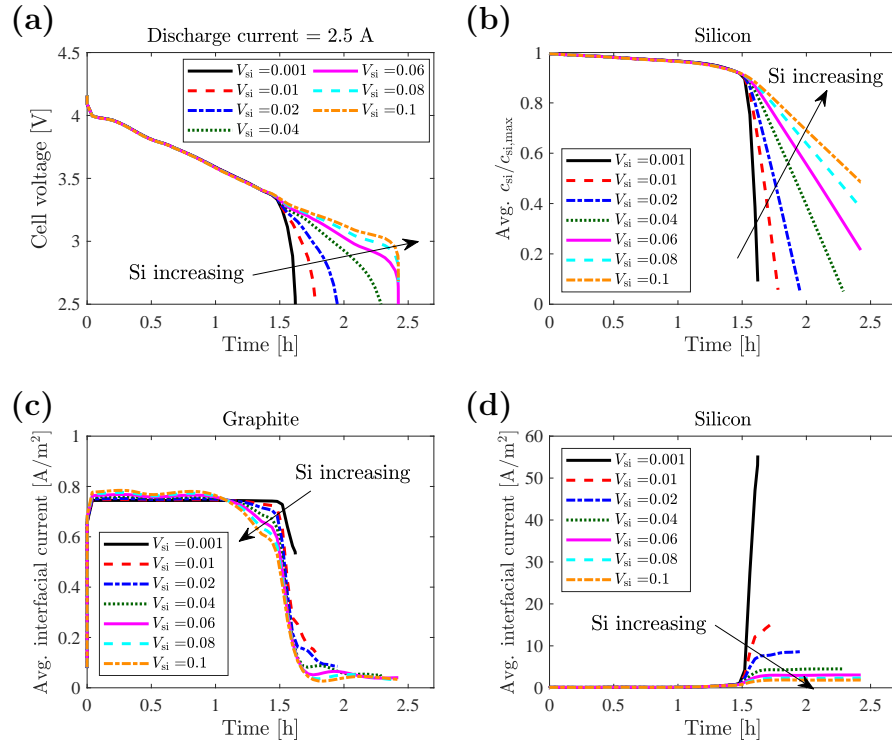
Figure 7: The influence of silicon volume fraction on the cell performance: (a) cell voltage, (b) averaged lithium concentration in silicon, averaged interfacial current density per area in (c) graphite and (d) silicon.

the reaction current, however at lower SOCs, as the degree of lithiation in graphite decreases, silicon then provides the majority of the reaction current. As the mass loading of silicon is significantly less than graphite (2 vs 98 vol%), resulting in a lower active surface area, the peak reaction current density is significantly higher than graphite.

At higher C-rates, further heterogenities are observed in the through thickness of the electrode. In the graphite phase, generally the peak reaction current densities are experienced at the separator-electrode side. In the silicon phase, at the end of discharge this is at the current collector-electrode side, highlighting the complex behaviour of composite electrodes.

Increasing the volume fraction of silicon has a positive influence on the reaction current density; reducing this due to the higher available surface area. Thus, this study provides key insights into the non-linear behaviour of composite electrodes. Deep depth of discharge cycling at high C-rates would suggest the silicon phase experiences extremely high current densities due to the non-linear splitting of the graphite-silicon contributions. The repercussion of which

18

would suggest that this would exasperate silicon phase lifetime due to mechanical pulverisation linked with (de)lithiation. These findings therefore allow for cell makers to better understand and control these types of lithium-ion batteries.

Acknowledgements

Declaration of competing interest

The authors declare no competing financial interests.

Appendix A. Open circuit potential

The OCPs are presented in Fig. A1 (a) for graphite [36] and silicon [13], from which interpolation functions for $\phi_{\text{g,ocp}}$ and $\phi_{\text{si,ocp}}$ are obtained. Then the incremental capacity analysis and differential voltage analysis are presented in Fig. A1 (b) and (c), respectively.
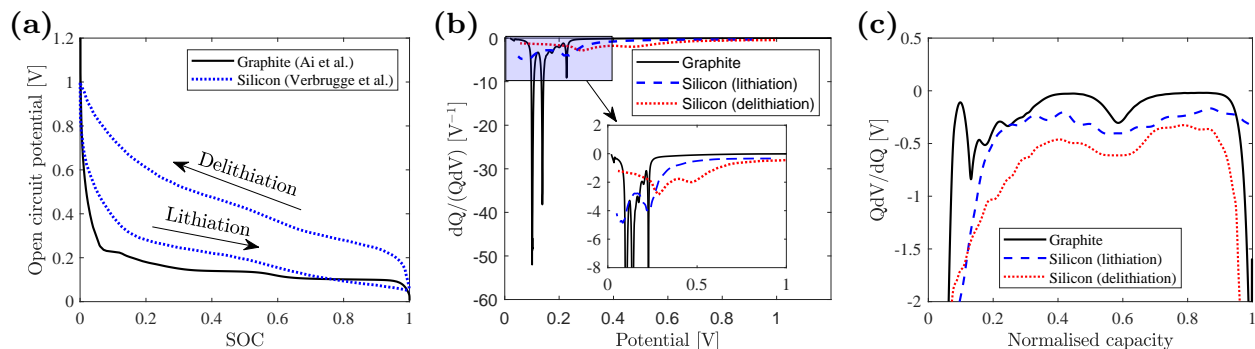

Figure A1: The electrochemical features of silicon [13] and graphite [36]: (a) the open circuit potential for graphite [36] and silicon [13] vs Li/Li$^+$, (b) incremental capacity analysis and (c) differential voltage analysis.

19

Appendix B. Experiment procedures

Experiments were performed on LG M50T (LG GBM50T2170) cylindrical lithium-ion batteries. These cells utilise a SiO_x-doped carbon anode alongside an NMC811 cathode, with a nominal capacity of 18.2 Wh (5 Ah).

All electrochemical data was recorded using a Biologic BCS-815 battery cycler with the accompanying BT-Lab software. Electrical connections to the cell were made via a spring-loaded cell holder, which provides a 4-point connection. The was housed inside a Binder thermal chamber (KB 23 cooling incubator), set to 298 K (fan speed of 100 %). The temperature of the cell was recorded using a K-type thermocouple adhered to the cell surface using Kapton tape, approximately half way along the axial direction. This was connected to the built-in thermocouple reader of the BCS-815 battery cycler, with temperature data recorded alongside the electrochemical data.

Prior to any discharge experiment, the cells were first charged to 100 % state of charge (SOC) using the standard charging procedure outlined in the cell specification sheet. This consisted of a constant current (CC) charge at 0.3 C (1.5 A) until the upper voltage limit of 4.2 V was reached, with a subsequent constant voltage (CV) charge at 4.2 V until the current dropped below C/100 (50 mA). This standard charge was always performed at a temperature of 298 K. The cell was then rested for 2 hours under open circuit conditions to allow the open circuit voltage (OCV) to equilibrate. We used this starting point to define 100 % SOC for subsequent discharge experiments, ensuring a consistent starting point between tests.

References

[1] Z. Liu, Q. Yu, Y. Zhao, R. He, M. Xu, S. Feng, S. Li, L. Zhou, L. Mai, Silicon oxides: A promising family of anode materials for lithium-ion batteries, Chem. Soc. Rev. 48 (1) (2019) 285–309. `doi:10.1039/c8cs00441b`.

[2] J. S. Edge, S. O'Kane, R. Prosser, N. D. Kirkaldy, A. N. Patel, A. Hales, A. Ghosh, W. Ai, J. Chen, J. Yang, S. Li, M. C. Pang, L. Bravo Diaz, A. Tomaszewska, M. W. Marzook, K. N. Radhakrishnan, H. Wang, Y. Patel, B. Wu, G. J. Offer, Lithium ion

battery degradation: what you need to know, Phys. Chem. Chem. Phys. 23 (14) (2021) 8200–8221. `doi:10.1039/d1cp00359c`.

[3] K. P. C. Yao, J. S. Okasinski, K. Kalaga, J. D. Almer, D. P. Abraham, Operando Quantification of (De)Lithiation Behavior of Silicon–Graphite Blended Electrodes for Lithium-Ion Batteries, Adv. Energy Mater. 9 (8) (2019) 1803380. `doi:10.1002/aenm.201803380`.

[4] C. H. Chen, F. Brosa Planella, K. O'Regan, D. Gastol, W. D. Widanage, E. Kendrick, Development of Experimental Techniques for Parameterization of Multi-scale Lithium-ion Battery Models, J. Electrochem. Soc. 167 (8) (2020) 080534. `doi:10.1149/1945-7111/ab9050`.

[5] X. H. Liu, L. Zhong, S. Huang, S. X. Mao, T. Zhu, J. Y. Huang, Size-dependent fracture of silicon nanoparticles during lithiation, Acs Nano 6 (2) (2012) 1522–1531. `doi:10.1021/nn204476h`.

[6] M. Pharr, Z. Suo, J. J. Vlassak, Measurements of the fracture energy of lithiated silicon electrodes of Li-Ion batteries, Nano Lett. 13 (11) (2013) 5570–5577. `doi:10.1021/nl403197m`.

[7] K. Zhao, M. Pharr, Q. Wan, W. L. Wang, E. Kaxiras, J. J. Vlassak, Z. Suo, Concurrent Reaction and Plasticity during Initial Lithiation of Crystalline Silicon in Lithium-Ion Batteries, J. Electrochem. Soc. 159 (3) (2012) A238–A243. `doi:10.1149/2.020203jes`.

[8] A. Sarkar, P. Shrotriya, A. Chandra, Fracture Modeling of Lithium-Silicon Battery Based on Variable Elastic Moduli, J. Electrochem. Soc. 164 (11) (2017) E3606—-E3612. `doi:10.1149/2.0631711jes`.

[9] B. Ding, X. Li, X. Zhang, H. Wu, Z. Xu, H. Gao, Brittle versus ductile fracture mechanism transition in amorphous lithiated silicon: From intrinsic nanoscale cavitation to shear banding, Nano Energy 18 (2015) 89–96. `doi:10.1016/j.nanoen.2015.10.002`.

[10] M. N. Obrovac, L. Christensen, Structural Changes in Silicon Anodes during Lithium Insertion/Extraction, Electrochem. Solid-State Lett. 7 (5) (2004) A93. `doi:10.1149/1.1652421`.

[11] W. J. Zhang, Lithium insertion/extraction mechanism in alloy anodes for lithium-ion batteries, J. Power Sources 196 (3) (2011) 877–885. `doi:10.1016/j.jpowsour.2010.08.114`.

[12] M. W. Verbrugge, D. R. Baker, X. Xiao, Q. Zhang, Y. T. Cheng, Experimental and theoretical characterization of electrode materials that undergo large volume changes and application to the lithium-silicon system, J. Phys. Chem. C 119 (10) (2015) 5341–5349. `doi:10.1021/jp512585z`.

[13] M. Verbrugge, D. Baker, X. Xiao, Formulation for the Treatment of Multiple Electrochemical Reactions and Associated Speciation for the Lithium-Silicon Electrode, J. Electrochem. Soc. 163 (2) (2016) A262–A271. `doi:10.1149/2.0581602jes`.

[14] Y. Jiang, G. Offer, J. Jiang, M. Marinescu, H. Wang, Voltage Hysteresis Model for Silicon Electrodes for Lithium Ion Batteries, Including Multi-Step Phase Transformations, Crystallization and Amorphization, J. Electrochem. Soc. 167 (13) (2020) 130533. `doi:10.1149/1945-7111/abbbba`.

[15] B. Lu, Y. Song, Q. Zhang, J. Pan, Y. T. Cheng, J. Zhang, Voltage hysteresis of lithium ion batteries caused by mechanical stress, Phys. Chem. Chem. Phys. 18 (6) (2016) 4721–4727. `doi:10.1039/c5cp06179b`.

[16] M. Wang, X. Xiao, Investigation of the chemo-mechanical coupling in lithiation/delithiation of amorphous Si through simulations of Si thin films and Si nanospheres, J. Power Sources 326 (2016) 365–376. `doi:10.1016/j.jpowsour.2016.07.011`.

[17] J. Guo, D. Dong, J. Wang, D. Liu, X. Yu, Y. Zheng, Z. Wen, W. Lei, Y. Deng, J. Wang, G. Hong, H. Shao, Silicon-Based Lithium Ion Battery Systems: State-of-the-Art from Half and Full Cell Viewpoint, Adv. Funct. Mater. 31 (34) (2021) 2102546. `doi:10.1002/adfm.202102546`.

[18] Y. N. Jo, Y. Kim, J. S. Kim, J. H. Song, K. J. Kim, C. Y. Kwag, D. J. Lee, C. W. Park, Y. J. Kim, Si-graphite composites as anode materials for lithium secondary batteries, J. Power Sources 195 (18) (2010) 6031–6036. `doi:10.1016/j.jpowsour.2010.03.008`.

[19] S. Müller, P. Pietsch, B. E. Brandt, P. Baade, V. De Andrade, F. De Carlo, V. Wood, Quantification and modeling of mechanical degradation in lithium-ion batteries based on nanoscale imaging, Nat. Commun. 9 (1) (2018) 1–8. `doi:10.1038/s41467-018-04477-1`.

[20] W. Li, K. Cao, H. Wang, J. Liu, L. Zhou, H. Yao, Carbon coating may expedite the fracture of carbon-coated silicon core-shell nanoparticles during lithiation, Nanoscale 8 (9) (2016) 5254–5259. `doi:10.1039/c5nr08498a`.

[21] W. Wu, M. Wang, J. Wang, C. Wang, Y. Deng, Green Design of Si/SiO 2 /C Composites as High-Performance Anodes for Lithium-Ion Batteries, ACS Appl. Energy Mater. 3 (4) (2020) 3884–3892. `doi:10.1021/acsaem.0c00300`.

[22] X. Shen, Z. Tian, R. Fan, L. Shao, D. Zhang, G. Cao, L. Kou, Y. Bai, Research progress on silicon/carbon composite anode materials for lithium-ion battery, J. Energy Chem. 27 (4) (2018) 1067–1090. `doi:10.1016/j.jechem.2017.12.012`.

[23] C. C. Nguyen, H. Choi, S.-W. Song, Roles of Oxygen and Interfacial Stabilization in Enhancing the Cycling Ability of Silicon Oxide Anodes for Rechargeable Lithium Batteries, J. Electrochem. Soc. 160 (6) (2013) A906–A914. `doi:10.1149/2.118306jes`.

[24] H. Takezawa, S. Ito, H. Yoshizawa, T. Abe, Surface composition of a SiOx film anode cycled in carbonate electrolyte for Li-ion batteries, Electrochim. Acta 229 (2017) 438–444. `doi:10.1016/j.electacta.2017.01.138`.

[25] D. Yao, J. Feng, J. Wang, Y. Deng, C. Wang, Synthesis of silicon anode binders with ultrahigh content of catechol groups and the effect of molecular weight on battery performance, J. Power Sources 463 (2020) 228188. `doi:10.1016/j.jpowsour.2020.228188`.

[26] P. Bärmann, M. Diehl, L. Göbel, M. Ruttert, S. Nowak, M. Winter, T. Placke, Impact of the silicon particle size on the pre-lithiation behavior of silicon/carbon composite materials

for lithium ion batteries, J. Power Sources 464 (2020) 228224. `doi:10.1016/j.jpowsour.2020.228224`.

[27] S. Dhillon, G. Hernández, N. P. Wagner, A. M. Svensson, D. Brandell, Modelling capacity fade in silicon-graphite composite electrodes for lithium-ion batteries, Electrochim. Acta 377 (2021) 138067. `doi:10.1016/j.electacta.2021.138067`.

[28] B. Liu, Y. Jia, J. Li, H. Jiang, S. Yin, J. Xu, Multiphysics coupled computational model for commercialized Si/graphite composite anode, J. Power Sources 450 (2020) 227667. `doi:10.1016/j.jpowsour.2019.227667`.

[29] S. Jung, Mathematical model of lithium-ion batteries with blended-electrode system, J. Power Sources 264 (2014) 184–194. `doi:10.1016/j.jpowsour.2014.04.072`.

[30] J. Marcicki, A. Bartlett, M. Canova, A. T. Conlisk, G. Rizzoni, Y. Guezennec, X. G. Yang, T. Miller, Characterization of Cycle-Life Aging in Automotive Lithium-Ion Pouch Cells, Ecs. Transactions. 50 (26) (2013) 235–247. `doi:10.1149/05026.0235ecst`.

[31] A. Bartlett, J. Marcicki, S. Onori, G. Rizzoni, X. G. Yang, T. Miller, Electrochemical Model-Based State of Charge and Capacity Estimation for a Composite Electrode Lithium-Ion Battery, Ieee T. Contr. Syst. T. (2015) 384–399.`doi:10.1109/TCST.2015.2446947`.

[32] L. Camacho-Solorio, M. Krstic, R. Klein, A. Mirtabatabaei, S. J. Moura, State Estimation for an Electrochemical Model of Multiple-Material Lithium-Ion Batteries, in: 2016 ASME Dyn. Syst. Control Conf. (Vol. 1), American Society of Mechanical Engineers, 2016. `doi:10.1115/DSCC2016-9877`.

[33] P. Albertus, J. Christensen, J. Newman, Experiments on and Modeling of Positive Electrodes with Multiple Active Materials for Lithium-Ion Batteries, J. Electrochem. Soc. 156 (7) (2009) A606. `doi:10.1149/1.3129656`.

[34] T. Chen, J. Wu, Q. Zhang, X. Su, Recent advancement of SiOx based anodes for lithium-ion batteries, J. Power Sources 363 (2017) 126–144. `doi:10.1016/j.jpowsour.2017.07.073`.

[35] M. Doyle, T. F. Fuller, J. Newman, Modeling of Galvanostatic Charge and Discharge of the Lithium/Polymer/Insertion Cell, J. Electrochem. Soc. 140 (6) (1993) 1526. `doi: 10.1149/1.2221597`.

[36] W. Ai, L. Kraft, J. Sturm, A. Jossen, B. Wu, Electrochemical Thermal-Mechanical Modelling of Stress Inhomogeneity in Lithium-Ion Pouch Cells, J. Electrochem. Soc. 167 (1) (2020) 013512. `doi:10.1149/2.0122001JES`.

[37] S. Yang, R. He, Z. Zhang, Y. Cao, X. Gao, X. Liu, CHAIN: Cyber Hierarchy and Interactional Network Enabling Digital Solution for Battery Full-Lifespan Management, Matter 3 (1) (2020) 27–41. `doi:10.1016/j.matt.2020.04.015`.

[38] S. Yang, Z. Zhang, R. Cao, M. Wang, H. Cheng, L. Zhang, Y. Jiang, Y. Li, B. Chen, H. Ling, Y. Lian, B. Wu, X. Liu, Implementation for a cloud battery management system based on the CHAIN framework, Energy and AI 5 (2021) 100088. `doi:10.1016/j.egyai. 2021.100088`.